doi:10.1093/plphys/kiab251 PLANT PHYSIOLOGY 2021: 187: 603–617

Plant Physiology®

Breakthrough Tech

Simultaneous imaging of ER and cytosolic Ca^{2+} dynamics reveals long-distance ER Ca^{2+} waves in plants

Francesca Resentini ,[1,‡] Matteo Grenzi ,[1,‡] Daniele Ancora ,[2] Mara Cademartori,[1] Laura Luoni ,[1] Marianna Franco ,[1] Andrea Bassi ,[2] Maria Cristina Bonza ,[1] and Alex Costa [1,3,*,†]

1 Department of Biosciences, University of Milan, Milan 20133, Italy
2 Department of Physics, Politecnico di Milano, Milan 20133, Italy
3 Institute of Biophysics, Consiglio Nazionale Delle Ricerche, Milan 20133, Italy

*Author for communication: alex.costa@unimi.it
†Senior author.
‡These authors contributed equally to this work (F.R. and M.G.).

A.C. and M.C.B. conceived the project with specific input from F.R., M.G., and A.B., M.G., and A.C. designed the experiments. F.R., M.C., and M.F. generated the constructs. F.R., M.G., and M.F. performed and analyzed the experiments. F.R. and L.L. generated the transgenic lines. D.A. and A.B. performed cross-correlation analyses of Figure 3 and temporal evolution of signals in Figure 4. A.C. and M.G. prepared the figures and videos. A.C. and M.C.B. wrote the manuscript with input from all coauthors. A.C. agrees to serve as the author responsible for contact and ensures communication.
The author responsible for distribution of materials integral to the findings presented in this article in accordance with the policy described in the Instructions for Author (https://academic.oup.com/plphys/pages/general-instructions) is: Alex Costa (alex.costa@unimi.it).

Abstract

Calcium ions (Ca^{2+}) play a key role in cell signaling across organisms. In plants, a plethora of environmental and developmental stimuli induce specific Ca^{2+} increases in the cytosol as well as in different cellular compartments including the endoplasmic reticulum (ER). The ER represents an intracellular Ca^{2+} store that actively accumulates Ca^{2+} taken up from the cytosol. By exploiting state-of-the-art genetically encoded Ca^{2+} indicators, specifically the ER-GCaMP6-210 and R-GECO1, we report the generation and characterization of an Arabidopsis (*Arabidopsis thaliana*) line that allows for simultaneous imaging of Ca^{2+} dynamics in both the ER and cytosol at different spatial scales. By performing analyses in single cells, we precisely quantified (1) the time required by the ER to import Ca^{2+} from the cytosol into the lumen and (2) the time required to observe a cytosolic Ca^{2+} increase upon the pharmacological inhibition of the ER-localized P-Type IIA Ca^{2+}-ATPases. Furthermore, live imaging of mature, soil-grown plants revealed the existence of a wounding-induced, long-distance ER Ca^{2+} wave propagating in injured and systemic rosette leaves. This technology enhances high-resolution analyses of intracellular Ca^{2+} dynamics at the cellular level and in adult organisms and paves the way to develop new methodologies aimed at defining the contribution of subcellular compartments in Ca^{2+} homeostasis and signaling.

Introduction

In animals, besides its role in protein secretion, the endoplasmic reticulum (ER) is a calcium ions (Ca^{2+}) store participating in the generation and shaping of stimulus-induced cytosolic Ca^{2+} increases (Soboloff et al., 2012). Moreover, in animals, Ryanodine (RyR) and inositol trisphosphate ($InsP_3R$) receptors are ER-localized, ligand-gated Ca^{2+} permeable channels that release Ca^{2+} into the cytosol (Foskett et al.,

Received February 02, 2021. Accepted May 12, 2021. Advance access publication May 29, 2021

2007), whereas the ER Ca^{2+} refilling is dependent on the activity of sarco/ER Ca^{2+}-ATPases (SERCA) and the stromal interaction molecule (STIM)–Orai protein complex (Soboloff et al., 2012). In plants, RyR, $InsP_3R$, and the STIM–Orai complex are not present (Edel et al., 2017). However, a battery of P-Type IIA (ER-type Ca^{2+}-ATPases, ECAs) and IIB (autoinhibited Ca^{2+} ATPases, ACAs) Ca^{2+}-ATPases are localized in the ER membranes and their primary function is to import Ca^{2+} into the ER lumen (Bonza and De Michelis, 2011; Bonza et al., 2013; Shkolnik et al., 2018). In addition, Ca^{2+}-permeable channels (e.g. cyclic nucleotide-gated channels) localized in the nuclear envelope (NE, which is in continuity with the ER; Charpentier et al., 2016; Leitão et al., 2019) and Ca^{2+}/cation transporters (e.g. CCXs) have been shown to participate in the regulation of Ca^{2+} transport across the ER membranes (Corso et al., 2018).

Ca^{2+} transport over the ER membrane was observed using purified microsomal vesicles loaded with the $^{45}Ca^{2+}$ isotope (Navazio et al., 2000). Later, by using Förster resonance energy transfer (FRET)-based genetically encoded Ca^{2+} indicator (GECI; SP-YC4.6 and calreticulin [CRT]-D4ER Cameleon) localized to the ER lumen, the ER resting Ca^{2+} concentration ($[Ca^{2+}]$) was measured in vivo in Arabidopsis (*Arabidopsis thaliana*) pollen tubes and in leaf and root cells (Iwano et al., 2009; Bonza et al., 2013; Tian et al., 2014). By using the ratiometric CRT-D4ER Cameleon, we previously reported, in root-tip cells, the ER Ca^{2+} dynamics in response to different stimuli, such as external ATP, L-glutamate, salt stress, and water potential gradient (Bonza et al., 2013; Corso et al., 2018; Shkolnik et al., 2018). Some of these data were later confirmed by Luo et al. (2020), who generated a new Arabidopsis line expressing the intensiometric ER-localized sensor R-CEPIA1er (Luo et al., 2020).

Overall, in plants, in vivo analyses of ER Ca^{2+} dynamics revealed that it primarily acts as a Ca^{2+} sink, thus contributing to the dampening of the Ca^{2+} transient (Bonza et al., 2013; Corso et al., 2018). However, ER can also work as a Ca^{2+} source, being responsible for the generation of a cytosolic Ca^{2+} transient (Shkolnik et al., 2018; Luo et al., 2020).

Here we report the successful use of spectral variants of the new generation of intensiometric single fluorescent protein GECIs (e.g. ER-GCaMP6-210 and R-GECO1) to perform simultaneous imaging of Ca^{2+} dynamics in the ER and cytosol. We demonstrate this method in single plant cells as well as in adult plants.

Results and discussion

Over the years, we have exploited the use of the ratiometric FRET-based CRT-D4ER Cameleon to study Ca^{2+} dynamics in the ER lumen of wild-type (WT) and mutant Arabidopsis plants (Bonza et al., 2013; Corso et al., 2018; Shkolnik et al., 2018). This ratiometric sensor proved to be highly reliable to highlight different ER $[Ca^{2+}]$ at resting and in reporting ER Ca^{2+} dynamics in response to various stimuli in different mutants (Corso et al., 2018; Shkolnik et al., 2018). However, in Arabidopsis, the use of the CRT-D4ER sensor showed some limitations. First, for reasons not yet investigated, the CRT-D4ER sensor showed a varying degree of silencing. Despite the use of different promoters and vector backbones, we failed to detect the expression of the sensor in adult Arabidopsis plants (A. Costa and L. Luoni, unpublished data). Only when we expressed the sensor in the *rdr6-11* Arabidopsis background, which is impaired in gene silencing (Peragine et al., 2004), we detected the sensor expression in leaves of adult plants (A. Costa and L. Luoni, unpublished data). Due to these limitations, we could only study the ER Ca^{2+} dynamics in young seedlings (Bonza et al., 2013; Corso et al., 2018; Shkolnik et al., 2018). Second, in some cases, we were unable to obtain knockout mutants expressing the sensor (Corso et al., 2018).

In order to choose a highly sensitive sensor to perform the analysis of ER Ca^{2+} in different cell types, which is also usable in a simple fluorescence microscopy setup, we searched the literature to find a suitable ER single fluorophore-based GECI. This class of GECIs are intensiometric Ca^{2+} sensors, based on a circularly permuted fluorescent protein (e.g. GFP (Green Fluorescent Protein), YFP (Yellow Fluorescent Protein), or mApple; Baird et al., 1999; Nakai et al., 2001; Zhao et al., 2011) fused at its C- and N-termini with the components of a Ca^{2+} sensing module (i.e. CaM domain and the M13 peptide). In the presence of Ca^{2+}, this causes tightening of the interaction between C- and N-termini of the fluorophore, leading to increased brightness. De facto, this interaction induces an alteration of the spectral properties of the fluorescent protein with a strong increase in the fluorescence emitted (Nakai et al., 2001). Recently, de Juan-Sanz et al. (2017), generated two ER-localized, low-affinity Ca^{2+} variants of the intensiometric single fluorophore-based GECI GCaMP6 (Chen et al., 2013), dubbed ER-GCaMP6-150 and ER-GCaMP6-210 (where numbers indicate the in vitro Kd for Ca^{2+} of the two sensors expressed in micromolar; de Juan-Sanz et al., 2017). Both sensors were found to be efficiently targeted to the ER lumen of animal cells and their sensitivity allowed the observation of a rapid Ca^{2+} accumulation in the axonal ER during an action potential firing (de Juan-Sanz et al., 2017). Remarkably, the two intensiometric GECIs, the ER-GCaMP3 variant and G-CEPIA1er, failed to reveal any signal in nerve terminals during activity, thus demonstrating a superior sensitivity of the ER-GCaMP6 sensors (de Juan-Sanz et al., 2017). Based on the fact that the CRT-D4ER, having an in vitro K_d for Ca^{2+} of 195 μM (Palmer et al., 2006; Greotti et al., 2016), efficiently reports ER Ca^{2+} dynamics in plant cells (Bonza et al., 2013), we decided to test the ER-GCaMP6-210 variant to overcome the previous failures of other Ca^{2+} ER sensors in plants.

To express the ER-GCaMP6-210 sensor in plants, we generated different constructs (see "Materials and methods") by placing its coding sequence under the control of two different constitutive promoters (i.e. CaMV35S and pUBQ10; Grefen et al., 2010; Amack and Antunes, 2020). The original ER-GCaMP6-210 harbors the signal peptide of CRT at the

N-terminus and the KDEL retention motif at the C-terminus which efficiently targeted the sensor to the ER of neuronal cells (de Juan-Sanz et al., 2017). To verify that the N- and C-terminal sequences were also sufficient to localize the sensor to the ER of plant cells, we transiently coexpressed the ER-GCaMP6-210 sensor with the ER marker nWAK2-mCherry-HDEL in *Nicotiana benthamiana* leaf epidermal cells (Nelson et al., 2007; Bonza et al., 2013; Supplemental Figure S1). The fluorescence emissions of ER-GCaMP6-210 and of the ER marker showed a clear merge in the cellular endomembrane system as well as in the NE (Supplemental Figure S1, D, H, and K). The perfect merge of the two signals was particularly clear at higher magnifications (Supplemental Figure 1, I–K). This experiment showed that the sensor was efficiently expressed under both promoters and that was properly localized to the ER (Supplemental Figure S1, A and E). When the ER-GCaMP6-210 was stably introduced in Arabidopsis Columbia 0 (Col-0) plants, the cellular fluorescence distribution was still clearly localized to the ER (Brandizzi et al., 2002; Bonza et al., 2013) and detected in both root and leaf cells (Supplemental Figure S2, A–D). Of note, the ER-GCaMP6-210 was efficiently expressed in guard cells where a neat signal in the NE was recognized (Supplemental Figure S2, G and I). We tested the functionality of the new sensor in both pCaMV35S- and pUBQ10-ER-GCaMP6-210 Arabidopsis lines, challenging seedlings with external ATP (0.1 mM) as an efficient and reliable stimulus known to trigger a cytosolic $[Ca^{2+}]$ ($[Ca^{2+}]_{cyt}$) increase in root-tip cells (Tanaka et al., 2010; Bonza et al., 2013; Behera et al., 2018). We performed parallel experiments using Arabidopsis seedlings expressing the cytosolic and nuclear-localized R-GECO1 sensor (Keinath et al., 2015). The first set of experiments were carried out following the same experimental design as that reported in Behera et al. (2018), where we made use of a custom perfusion setup for in vivo wide-field fluorescence microscopy imaging in Arabidopsis roots (Behera and Kudla, 2013). A 3-min pulsed ATP administration to the seedlings expressing ER-GCaMP6-210 and R-GECO1 triggered clear fluorescence increases that reflected a transient rise of $[Ca^{2+}]_{ER}$ and $[Ca^{2+}]_{cyt}$ (Supplemental Figure S3A). The $[Ca^{2+}]_{ER}$ peak (Supplemental Figure S3B) temporally followed the $[Ca^{2+}]_{cyt}$ rise (Supplemental Figure S3C) and the ER showed a slower recovery to the prestimulus $[Ca^{2+}]_{ER}$ compared to the $[Ca^{2+}]_{cyt}$ (Supplemental Figure S3D). Importantly, performing a comparison between seedlings expressing the ER-GCaMP6-210 with those expressing the Cameleon CRT-D4ER (Bonza et al., 2013) revealed that the two sensors reported similar $[Ca^{2+}]_{ER}$ dynamics in response to ATP, with no difference both in the times at which the $[Ca^{2+}]_{ER}$ peak was reached (Supplemental Figure S3, E and G) and the times of recovery (Supplemental Figure S3H). Instead, the ER-GCaMP6-210 exhibited a significantly increased signal change compared with the CRT-D4ER (Supplemental Figure S3F). It has been reported that most of the single fluorescent protein GECIs show pH sensitivity (Zhao et al., 2011; Keinath et al., 2015). On the other hand, pH has a minor effect on the readout of ratiometric FRET-based sensors like Cameleon (Nagai et al., 2004; Behera et al., 2018; Grenzi et al., submitted for publication). The high similarity of Ca^{2+} dynamics monitored by using the ER-GCaMP6-210 and CRT-D4ER suggests that in the ER lumen, the probable pH change, possibly dependent on a coupled Ca^{2+}/H^{+} transport occurring across the ER membrane (e.g. ECAs and ACAs exchange Ca^{2+} with H^{+} [Bonza and De Michelis, 2011; Resentini et al., 2021]), does not seem to affect the ER-GCaMP6-210 sensor readout. To further test the functionality of the ER-GCaMP6-210 sensor, we treated the seedlings (in both pCaMV35S- and pUBQ10 lines) with 0.01 mM naphthalene-1-acetic acid (NAA; Behera et al., 2018). A 3-min pulsed NAA treatment was also efficient to induce a transient accumulation of Ca^{2+} in both compartments (Supplemental Figure S3, I and J), with the ER Ca^{2+} accumulation showing slower dynamics compared to the cytosol concerning both the maximum peak (Supplemental Figure S3K) and the recovery of the prestimulus $[Ca^{2+}]$ (Supplemental Figure S3L).

Overall, whereas different ATP- and NAA-induced Ca^{2+} dynamics in the cytosol were well documented (Waadt et al., 2017; Behera et al., 2018), these new data showed that different dynamics were also detectable in the ER (Supplemental Figure S3, A and I). Specifically, in response to NAA the Ca^{2+} (expressed as $\Delta F_{max}/F_0$) in the ER peak and the time when it was reached was smaller (e.g. 0.37 ± 0.11 for NAA versus 1.47 ± 0.45 for ATP with the pUBQ10-ER-GCaMP6-210 line) and delayed (e.g. 157 ± 32 for NAA versus 129.2 ± 44 for ATP with the pUBQ10-ER-GCaMP6-210 line), respectively, compared to the one measured with the ATP treatment (Supplemental Figure S3, B, C, J, and K). Noticeably, this new set of results confirmed previously published data showing that the Ca^{2+} accumulation in the ER follows the cytosolic Ca^{2+} transient, again supporting a role of ER as a Ca^{2+} sink in response to stimuli that induce a $[Ca^{2+}]_{cyt}$ increase (Bonza et al., 2013; Corso et al., 2018).

Based on this first series of results, we felt confident that the ER-GCaMP6-210 sensor, despite the oxidative environment of the plant ER lumen (Aller et al., 2013) and the lower pH (Martinière et al., 2013), efficiently reports $[Ca^{2+}]_{ER}$ dynamics in accordance with what was reported in animal neurons (de Juan-Sanz et al., 2017). Therefore, having demonstrated the functionality of the new sensor in monitoring ER Ca^{2+} dynamics, we explored the possibility of performing simultaneous imaging of Ca^{2+} in ER and cytosol. To this end, we crossed both the pCaMV35S-ER-GCaMP6-210 and pUBQ10-ER-GCaMP6-210 Arabidopsis lines with the pUBQ10-R-GECO1 line (Zhao et al., 2011; Keinath et al., 2015) and selected seedlings showing both types of fluorescence (Figure 1, A–D; Supplemental Figure S4). As the stable expression of GECIs might affect plant growth and development (De Col et al., 2017; Waadt et al., 2017), before proceeding with further analyses, we phenotypically characterized the Arabidopsis lines expressing the ER-

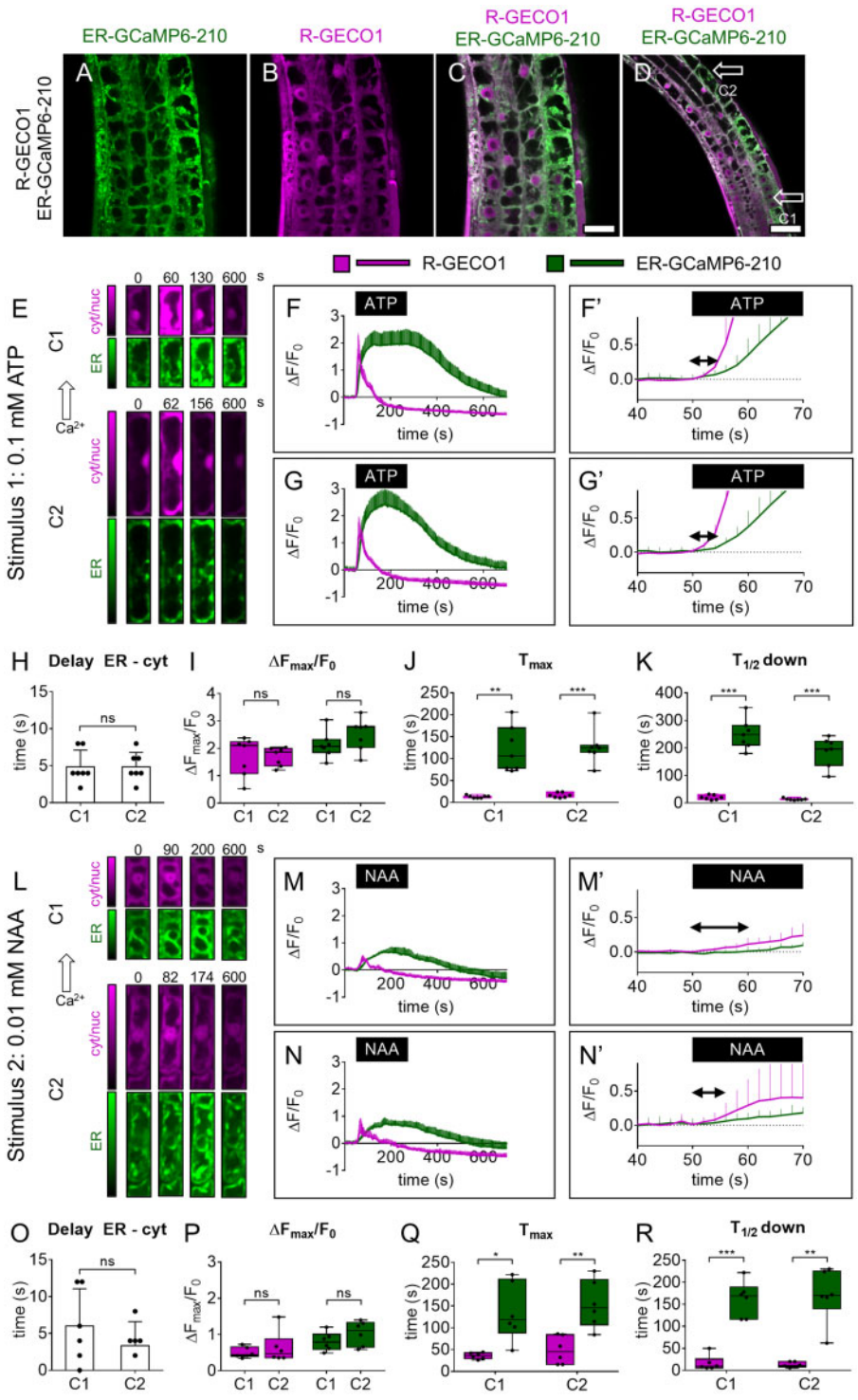

Figure 1 Simultaneous cytosolic and ER Ca^{2+} analyses in root tip at the single-cell level. A–D, Images of root-tip cells of a representative pUBQ10-ER-GCaMP6-210 × pUBQ10-R-GECO1 seedling. A, Green: ER-GCaMP6-210 fluorescence. B, Magenta: R-GECO1 fluorescence. C, Overlay of (A) and (B). Scale bar 25 μm. D, Lower magnification image of (C). Scale bar 50 μm. E, Exemplary false-color images illustrate R-GECO1 (magenta) and ER-GCaMP6-210 (green) of cell 1 (C1) and cell 2 (C1) in root tips of seedlings expressing simultaneously the two Ca^{2+} sensors at steady-state and during the Ca^{2+} transient induced by the treatment with 0.1 mM ATP for 3 min. F, R-GECO1 and ER-GCaMP6-210 normalized fluorescence changes of C1 over the time acquired under continuous perfusion and treated with 0.1 mM ATP for 3 min, as indicated by the black box on the *x*-axis. F′, same as panel (F) but *x*-axis, *y*-axis scales, and ranges adjusted. G, R-GECO1 and ER-GCaMP6-210 normalized fluorescence changes of C2 over the time acquired under continuous perfusion and treated with 0.1 mM ATP for 3 min, as indicated by the black box on the *x*-axis. G′ same as panel (G) but *x*-axis, *y*-axis scales, and ranges adjusted. The double arrow in (F′) and (G′) indicates the delay time quantified in (H). H, Mean delay of the fluorescence increase of the ER-GCaMP6-210 compared to the fluorescence change of the R-GECO1 for C1 and C2 following 0.1 mM ATP administration. I, Maximal peaks of ER-GCaMP6-210 and R-GECO1 fluorescence signals for C1 and C2 after 0.1 mM ATP

GCaMP6-210 alone alongside those coexpressing the R-GECO1. We measured seedling root length, rosette size, silique length, and the number of seeds per silique of independent pCaMV35S-ER-GCaMP6-210, pUBQ10-ER-GCaMP6-210, and the R-GECO1 crossed lines. By comparing these parameters with the Col-0 WT, we did not observe any gross phenotypic differences in all sensor lines tested (Supplemental Figure S5, A–D), with only the pCaMV35S-ER-GCaMP6-210 line showing slightly reduced silique length and seed number (Supplemental Figure S5, C and D).

The proper expression of the ER-GCaMP6-210 under the control of the pUBQ10 promoter both alone (Supplemental Figure S2) and coexpressed with the R-GECO1 (Figure 1, A–D; Supplemental Figure S4), together with the lack of negative effects on plant growth and development (Supplemental Figure S5), prompted us to choose the pUBQ10-ER-GCaMP6-210 × pUBQ10-R-GECO1 line to carry out the simultaneous imaging of Ca^{2+} dynamics in the two cellular compartments.

To prove the validity, usability, and advantages of this new dual biosensor line, we pursued two different approaches as follows: (1) high spatiotemporal resolution Ca^{2+} imaging analyses in single cells and (2) low-magnification Ca^{2+} imaging analyses in adult mature plants.

Initially, we demonstrated the reliability of ATP and NAA to induce a transient Ca^{2+} accumulation in the cytosol and ER (Supplemental Figure S3). Those experiments were carried out by means of a wide-field microscope which, given its poor optical sectioning, provides averaged responses on several root-tip cells (Costa et al., 2013; Vigani and Costa, 2019). To perform single-cell analyses in seedling root tips, we made use of a spinning disk confocal. We independently acquired the ER-GCaMP6-210 and R-GECO1 fluorescence switching between GFP and Red Fluorescence Protein (RFP) filters: the delay between the emissions was <600 ms and the images were acquired every 2 s (see "Materials and methods"). For every experiment, we treated Arabidopsis root tips with 0.1 mM ATP or 0.01 mM NAA pulsed for 3 min using the same perfusion setup described above and we analyzed two different independent cell types (cell 1, C1, and cell 2, C2 in Figure 1; Figure 1, E and L; Supplemental Movie S1). Even at the single-cell level, the ER Ca^{2+} accumulation temporally followed the cytosolic increase (Figure 1, F, G, M, and N), showing a delayed maximum peak and a slower recovery time (Figure 1, H, J, K, O, Q, and R). It is noteworthy that the simultaneous imaging of the two compartments allowed us to precisely and directly determine the time delay between the beginning of the $[Ca^{2+}]_{cyt}$ increase and the following $[Ca^{2+}]_{ER}$ accumulation. This delay turned out to be, for both treatments, around 4–5 s (4.8 ± 2.2 s for ATP and 3.7 ± 2.6 for NAA; Figure 1, H and O). Aside from the ability to report different ER Ca^{2+} dynamics in response to different stimuli, this approach allowed us to measure the time required by the ER to import Ca^{2+} in response to a cytosolic Ca^{2+} increase; thus, it represents an in vivo measurement of the activity of ER-localized Ca^{2+}-transporters (e.g. ER-localized ACAs and ECAs; Bonza and De Michelis, 2011). To assess in vivo the contribution of ECAs in the active import of Ca^{2+} into the ER lumen, and their impact on the cytosolic Ca^{2+} homeostasis, we used cyclopiazonic acid (CPA). CPA is a nonfluorescent inhibitor of SERCA-like Ca^{2+}-ATPases including plant P-Type IIA ECAs (Liang and Sze, 1998). We treated Arabidopsis root tips of the dual sensor line with 25-μM CPA pulsed for 3 min and analyzed simultaneously in the same cell (Figure 2, A and B) both the $[Ca^{2+}]_{ER}$ and $[Ca^{2+}]_{cyt}$ dynamics (Figure 2C). Since we expected to have a CPA-dependent decrease in the ER-GCaMP6-210 fluorescence, to avoid bleaching of the sensor which might affect the measurement, we acquired images every 5 s instead of 2 s as for the experiments reported in Figure 1. The CPA administration determined a quick and sustained decrease of ER-GCaMP6-210 fluorescence, indicative of an $[Ca^{2+}]_{ER}$ depletion. The ER Ca^{2+} depletion was followed by a transient increase of $[Ca^{2+}]_{cyt}$ (Figure 2C). The treatment with DMSO (dimethyl sulfoxide) alone (used as a solvent for CPA) did not have any effect (dashed lines in Figure 2C′), demonstrating that the observed response was specific to CPA treatment. Based on these data, we measured the time between the initial decrease of $[Ca^{2+}]_{ER}$ and the increase in $[Ca^{2+}]_{cyt}$ that was quantified in 14 ± 9 s (Figure 2, D and E). Interestingly, the CPA washout did not allow the recovery of $[Ca^{2+}]_{ER}$ indicating that once the inhibitor has entered the cell it cannot be quickly removed and that the ER-localized pumps are

administration. J, Time required to reach maximal peaks of ER-GCaMP6-210 and R-GECO1 fluorescence emissions for C1 and C2 after stimulus administration. K, Time required to pass half-maximal ER-GCaMP6-210 and R-GECO1 fluorescence signals during recovery after the stimulus. $n = 7$. L, Exemplary false-color images illustrate R-GECO1 (magenta) and ER-GCaMP6-210 (green) of C1 and C2 in root tips of seedlings expressing simultaneously the two Ca^{2+} sensors, at steady-state and during the Ca^{2+} increase induced by the treatment with 0.01 mM NAA for 3 min. M, R-GECO1 and ER-GCaMP6-210 normalized fluorescence changes of C1 over the time acquired under continuous perfusion and treated with 0.01 mM NAA for 3 min, as indicated by the black box on the *x*-axis. M′, Same as panel (M) but *x*-axis, *y*-axis scales, and ranges adjusted. N, R-GECO1 and ER-GCaMP6-210 normalized fluorescence changes of C2 over the time acquired under continuous perfusion and treated with 0.01 mM NAA for 3 min, as indicated by the black box on the *x*-axis. N′, same as panel (N) but *x*-axis, *y*-axis scales, and ranges adjusted. The double arrow in (M′) and (N′) indicates the delay time quantified in (O). O, Mean delay of the fluorescence increase of the ER-GCaMP6-210 compared to the fluorescence change of the R-GECO1 for C1 and C2 following 0.01 mM NAA administration. P, Maximal peaks of ER-GCaMP6-210 and R-GECO1 fluorescence signals for C1 and C2 after 0.01 mM NAA administration. Q, Time required to reach maximal peaks of ER-GCaMP6-210 and R-GECO1 fluorescence signals for C1 and C2 after stimulus administration. R, Time required to pass half-maximal ER-GCaMP6-210 and R-GECO1 fluorescence emissions during recovery after the stimulus. $n = 6$. Error bars = SD, ns = not significant, $^{*}P \leq 0.05$, $^{**}P \leq 0.005$, $^{***}P \leq 0.0005$ (Student's *t* test).

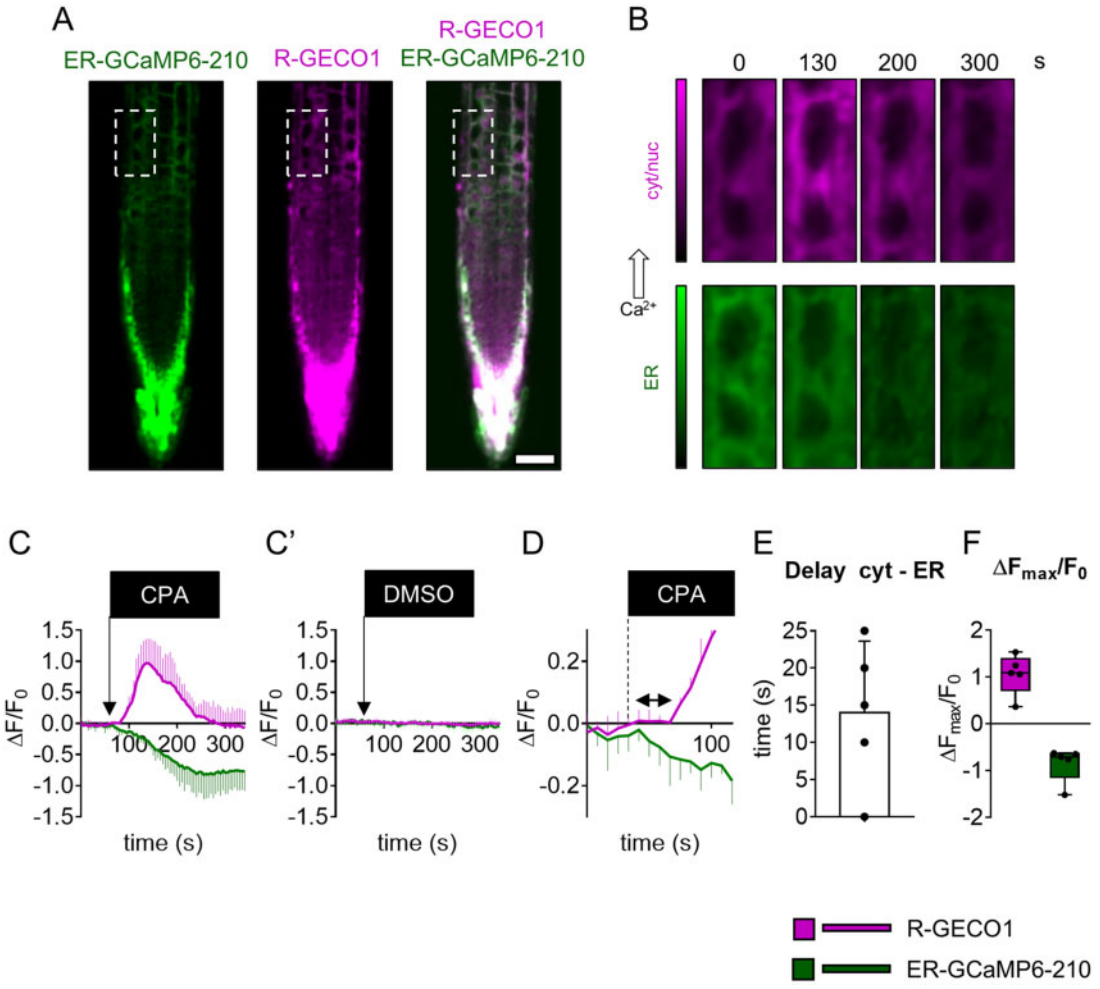

Figure 2 Simultaneous cytosolic and ER Ca^{2+} analyses in root-tip cells treated with the P-Type IIA inhibitor CPA. A, Green: ER-GCaMP6-210 fluorescence, magenta: R-GECO1 fluorescence, and overlay. Scale bar 50 μm. B, Examples of false-color images illustrate R-GECO1 (magenta) and ER-GCaMP6-210 (green) of the selected cell (dashed rectangle in A) in root tips of seedlings expressing simultaneously the two Ca^{2+} sensors at steady-state and during the Ca^{2} treatment with 25 μM CPA for 3 min. C, R-GECO1 and ER-GCaMP6-210 normalized fluorescence changes of the selected cell over the time acquired under continuous perfusion and treated with 25 μM CPA for 3 min, as indicated by the black box on the *x*-axis. C′, R-GECO1 and ER-GCaMP6-210 normalized fluorescence of the selected cell over the time acquired under continuous perfusion and treated with DMSO (the CPA solvent) as a control for 3 min, as indicated by the black box on the *x*-axis. D, same as panel (C) but *x*-axis, *y*-axis scales, and ranges adjusted. The double arrow in (D) indicates the delay time quantified in (E). E, Mean delay of the fluorescence increase of the R-GECO1 following the ER-GCaMP6-210 fluorescence decrease. F, The maximal peak of R-GECO1 and the minimal level of ER-GCaMP6-210 fluorescence signals for the selected cells after CPA administration. $n = 5$. Error bars = SD.

probably kept in an inactive state. Based on this latter result, we can claim that a decreased activity of the ECAs is sufficient to trigger a cytosolic Ca^{2+} increase (Figure 2F), and thus that the ER can potentially work as a cytosolic Ca^{2+} source in signaling processes. At the same time, this experiment underlines the key role played by CPA-sensitive Ca^{2+} transporters for the maintenance of ER Ca^{2+} homeostasis, confirming the data previously obtained with the CRT-D4ER line (Bonza et al., 2013). Nonetheless, this result demonstrates that other Ca^{2+} transporters, such as the ACAs and Ca^{2+} exchangers localized to the ER, tonoplast, and PM could be responsible for the observed recovery of the resting $[Ca^{2+}]_{cyt}$ (Resentini et al., 2021).

We can, therefore, foresee that this new dual sensor line will constitute a useful tool to study in planta, and in different tissues or cell types at high spatiotemporal resolution, the ER/cytosolic Ca^{2+} handling in response to different stimuli, in different genetic backgrounds, or following pharmacological treatments.

Although the experiments carried out in root cells reported ER and cytosolic Ca^{2+} transients in response to the perception of an exogenously applied stimulus or following a pharmacological treatment, we also wanted to investigate the ER/cytosolic Ca^{2+} dynamics with single-cell resolution during a developmental process, such as the pollen tube growth (Feijó et al., 2004), where a role of ER in the regulation of Ca^{2+} signaling has been suggested (Iwano et al., 2009, Barberini et al., 2018; Ishka et al., 2021). We collected pollen grains from flowers of the pUBQ10-ER-GCaMP6-210 × pUBQ10-R-GECO1 mature plants and let

them germinate in vitro as previously described (Schoenaers et al., 2017). We visually inspected the germinated pollen grains and selected those showing both fluorescence signals. We then followed their in vitro growth, acquiring images every 2 s and measuring the fluorescence intensities of both sensors in a region of interest (ROI) "a" drawn in the tip region just underneath the clear zone (Figure 3, A, B, and G; Supplemental Movie S2A). In ROI "a," the R-GECO1 revealed the typical tip cytosolic Ca^{2+} oscillations (Figure 3, G and G′; Supplemental Movie S2A) observed when pollens from different species germinate and grow in vitro (Damineli et al., 2017; Schoenaers et al., 2017; Barberini et al., 2018; Li et al., 2021). Pollen tubes showed a tip growth with an average speed of 0.033 ± 0.015 μm s^{-1} with cytosolic Ca^{2+} oscillations having an averaged frequency of 0.03 ± 0.01 Hz (Figure 3, G and G′). These data are consistent with previous reports (Iwano et al., 2009, Damineli et al., 2017; Schoenaers et al., 2017) and confirm that, in vitro, the pollens did not have growth defects. This holds also true in vivo since no alterations were observed in silique length and seed number (Supplemental Figure S5, C and D). The ER-GCaMP6-210 fluorescence in the ROI "a‴ also showed an oscillating behavior (Figure 3, G and G′), revealing the possible existence of $[Ca^{2+}]_{ER}$ oscillations which might, therefore, correspond with the tip cytosolic Ca^{2+}, which is known to be dependent on an influx of extracellular Ca^{2+} (Holdaway-Clarke et al., 1997). To investigate this possibility, we performed a normalized cross-correlation analysis between the R-GECO1 and the ER-GCaMP6-210 fluorescence signals. This analysis revealed a peak value of 0.28 ± 0.11 (Figure 3H) with a global temporal lag of 6 ± 2 s (Figure 3I) and an average oscillation time of 30 ± 11 s (Figure 3J), thus supporting a correlation between the two parameters. However, the combined effects of the continuous movement of the ER membranes, observed in the apex of the pollen tube (see the analyzed ROI "a‴ and the kymograph in Figure 3D; Lovy-Wheeler et al., 2007), and the intensiometric nature of the sensors do not make us confident to ascribe both the increase and decrease of the ER-GCaMP6-210 fluorescence uniquely to the sole change in the $[Ca^{2+}]_{ER}$. In this case, the use of a ratiometric sensor, such as the Cameleon CRT-D4ER, would probably help, but at present, we do not have a line expressing simultaneously the CRT-D4ER and the R-GECO1 in pollen. Nevertheless, the kymographs extracted for both fluorescence emissions of the representative pollen tube (Figure 3, D−F) revealed that an increase in the R-GECO1 and ER-GCaMP6-210 signals spread within the shank toward the grain (Figure 3, D and K; Supplemental Movie S2B), allowing us to quantify the R-GECO1 and ER-GCaMP6-210 fluorescence emissions in a second ROI "b" drawn in a region of the pollen shank where the movement of the ER membranes was limited (Figure 3, A, B, D, and E). Only a subpopulation of growing pollen tubes showed such cytosolic Ca^{2+} transients in the shank (ROI "b"), but when a change of R-GECO1 fluorescence was observed (Figure 3, K and K′), a clear increase of ER-GCaMP6-210 fluorescence was present, which followed the cytosolic signal with an average delay of 3.2 ± 1.1 s (Figure 3L). Moreover, similar to what was observed in root-tip cells, the ER-GCaMP6-210 fluorescence showed a more sustained increase compared with the cytosolic one (Figure 3M). Based on these observations, we suggest that the variation of ER-GCaMP6-210 fluorescence in the shank faithfully reported a change in the ER $[Ca^{2+}]$ and was not affected by heterogeneity in volume and concentration of the sensor.

In conclusion, although the ER-GCaMP6-210 allows efficient measurement of ER Ca^{2+} dynamics in pollen tubes, the data obtained by the analyses of the tip region should be taken with care. Nevertheless, we believe that this dual sensor line will be instrumental to reevaluate, besides CPA, the action of a series of inhibitors, known to affect the ER Ca^{2+} release in animal cells (e.g. 2-aminoethoxydiphenyl borate, heparin, and caffeine), that have also been shown to impact the cytosolic tip Ca^{2+} gradient and growth of pollen tubes in different species (e.g. *Solanum lycopersicum*, *Papaver rhoeas*, *Nicotiana tabacum*; Franklin-Tong et al., 1996; Barberini et al., 2018; Li et al., 2021).

The successful detection of single FP GECIs fluorescence (Vincent et al., 2017; Nguyen et al., 2018; Toyota et al., 2018) achieved with simple fluorescence microscopes (e.g. fluorescent stereomicroscopes) made us confident that this dual sensor line could also allow imaging of ER and cytosolic Ca^{2+} dynamics in adult mature plants. Therefore, we imaged 3-week-old Col-0 pUBQ10-ER-GCaMP6-210 × pUBQ10-R-GECO1 plants grown in soil, using a fluorescent stereomicroscope equipped with GFP and RFP filters (Figure 4, A–C). A rosette leaf was wounded by a tweezer according to Nguyen et al. (2018) and sensors' fluorescence emissions were monitored and quantified both in the wounded (local, l) and in a distal (d) leaf (Figure 4, A–D). The wounding induced both a cytosolic and ER Ca^{2+} increase in the local leaf, occurring primarily in the vasculatures and spreading within the leaf lamina and the petiole, eventually reaching a distal leaf (Figure 4, D–G; Supplemental Movie S3). Note that the drop of the initial fluorescence signals for both sensors, detectable in the local and distal leaves, was due to the movement of the entire plant when touched with the tweezer (red arrow in Figure 4F; Supplemental Movie S3). Whereas the cytosolic Ca^{2+} increase was expected to occur both in the wounded leaf and in the distal one (Mousavi et al., 2013; Nguyen et al., 2018), the wounding-induced ER Ca^{2+} accumulation in both sites was a novel observation, demonstrating that the magnitude of the cytosolic Ca^{2+} increase (Figure 4H) was sufficient to trigger the $[Ca^{2+}]_{ER}$ accumulation. Similar to what was observed in the previous experiments, the $[Ca^{2+}]_{ER}$ increase temporally followed the cytosolic one (Figure 4I), being also more sustained (Figure 4, F and G). To further analyze the representative experiment, we visually represented the temporal progression of the cytosolic and ER Ca^{2+} accumulation (Figure 4, L and M) by using false colors, representing by each color the time at which the maximum intensity in fluorescence occurred.

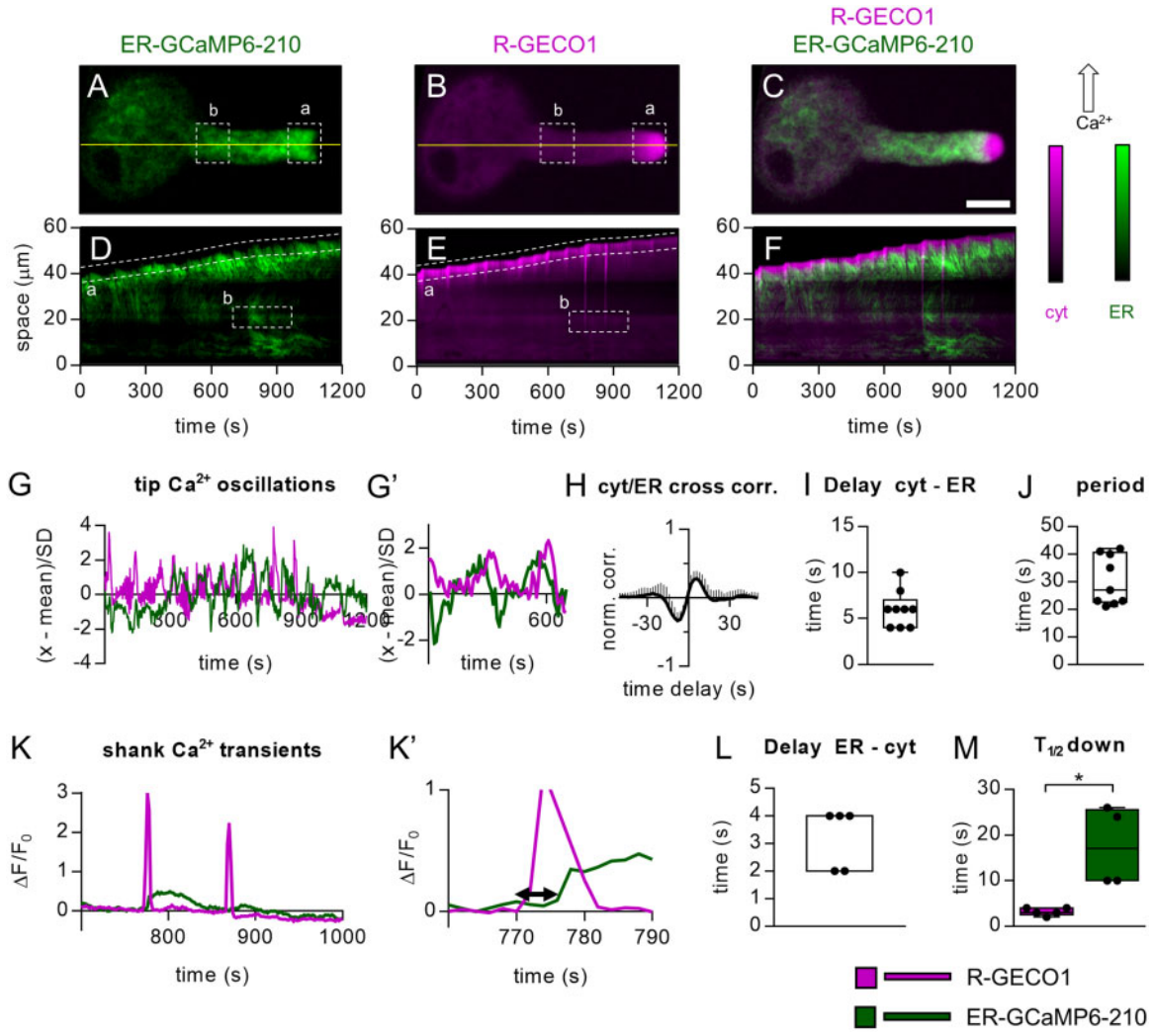

Figure 3 Simultaneous ER-GCaMP6-210 and R-GECO1 fluorescence signals in growing pollen tubes. A–C, Images of a representative pollen tube. A, Green: ER-GCaMP6-210 fluorescence. B, Magenta: R-GECO1 fluorescence. C, Overlay of (A) and (B). Scale bar 20 µm. D–F, Kymograph extracted from both fluorescence signals frames by observing the temporal evolution of the pixel line highlighted in yellow. D, Kymograph of 1,200 s acquisitions extracted for the R-GECO1 images. E, Kymograph of 1,200 s acquisitions extracted for the ER-GCaMP6-210 images. F, Overlay of (D) and (E). (a) = selected ROI for analyses of pollen tube tip fluorescence signals. (b) selected ROI for analyses of pollen tube shank fluorescence signals. G, Representative oscillations of ER-GCaMP6-210 and R-GECO1 fluorescences in the tip (ROI "a"). G′, same as panel (G) but *x*-axis, *y*-axis scales, and ranges adjusted. H, Normalized cross-correlation analysis between R-GECO1 and ER-GCaMP6-210 averaged in temporal sliding windows of 80 s over $n = 9$ measurements. The peak-value is 0.28 ± 0.11, and it is reached at positive delays, implying that the fast oscillations in the cytosol (R-GECO1) are anticipated by the ones in the ER (ER-GCaMP6-210). I, Distribution of the average delays by locating in time the maximum of the cross-correlations, for each experiment considered. The global temporal lag is 6 ± 2 s. J, Distribution of the period of the fast oscillations in the ER/Cytosol. It is defined by doubling the temporal distance at which the signals correlate (maximum in G) and anti-correlates (minimum). The average is 30 ± 11 s. K, Representative ER-GCaMP6-210 and R-GECO1 fluorescences in the shank (ROI "b"). K′, same as part (K) but *x*-axis, *y*-axis scales and ranges adjusted. The double arrow in (K′) indicates the delay time quantified in (L). L, Mean delay of the fluorescence increase of the ER-GCaMP6-210 compared to the fluorescence change of the R-GECO1. M, Time required to pass half-maximal ER-GCaMP6-210 and R-GECO1 fluorescence emissions during recovery after the spike. $n = 5$. Error bars = SD, $^*P \leq 0.05$ (Student's *t* test).

Pixel by pixel, the color was weighted by the absolute value achieved: the brighter the color, the higher the signal. Early signal peaks are labeled with blue color, fading to red and green for middle to late responses, respectively, thus presenting an overall idea about the signal propagation throughout the whole plant (Figure 4, L and M).

In conclusion, this latter result reports the existence of a long-distance ER Ca^{2+} wave induced by wounding that travels from leaf to leaf and temporally follows the cytosolic Ca^{2+} wave.

Conclusions

In this article, we report the generation of a new Arabidopsis line expressing both ER-GCaMP6-210 and R-GECO1 GECIs for the simultaneous in vivo imaging of Ca^{2+}

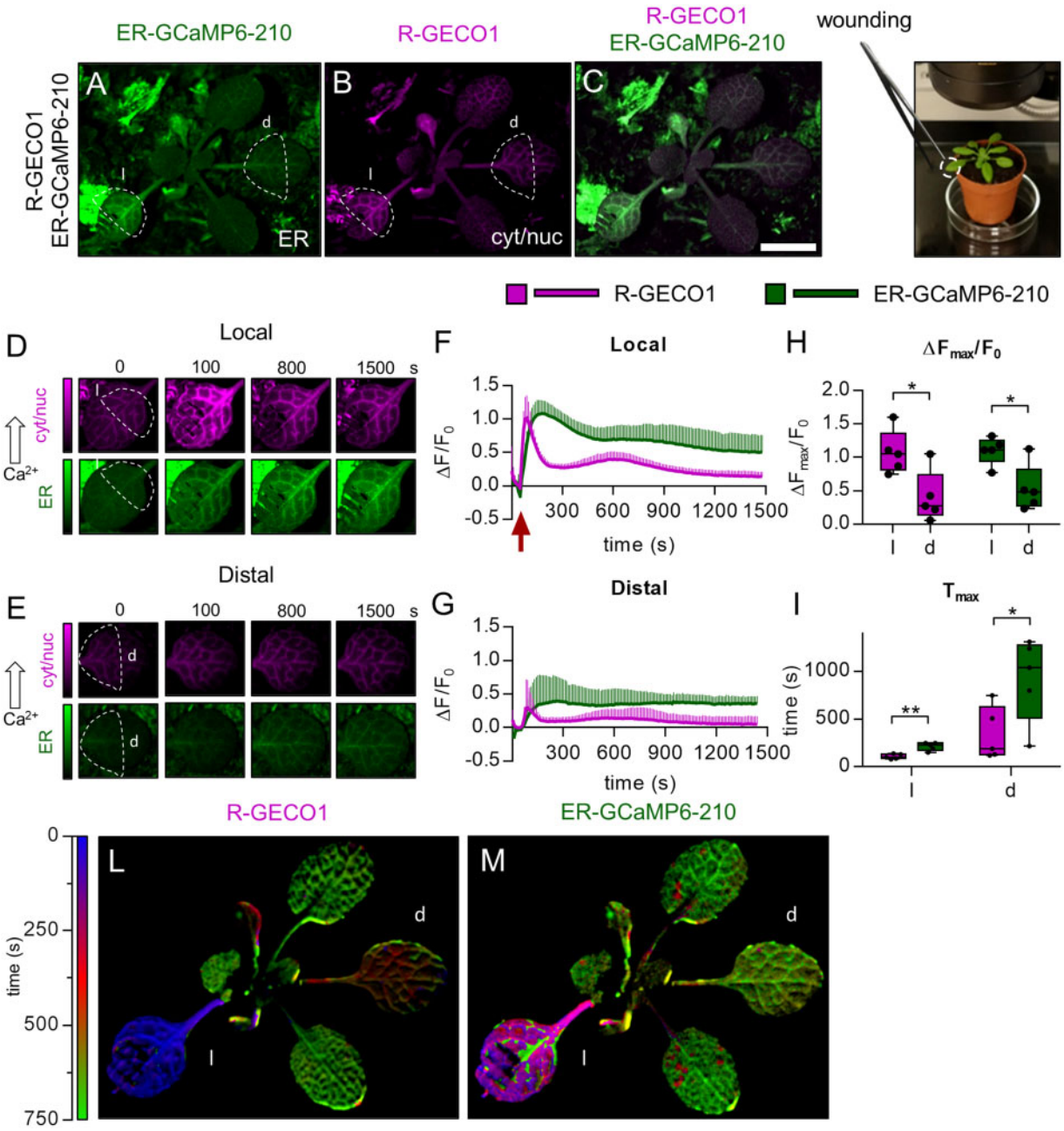

Figure 4. Simultaneous cytosolic and ER Ca^{2+} analyses in leaves of adult plants challenged with leaf wounding. A–C, Images of a representative pUBQ10-ER-GCaMP6-210 x pUBQ10-R-GECO1 mature plant. A, Green: ER-GCaMP6-210 fluorescence. B, Magenta: R-GECO1 fluorescence. C, Overlay of (A) and (B). Scale bar 1 mm. D, Examples of false-color images illustrate R-GECO1 (magenta) and ER-GCaMP6-210 (green) in a local wounded leaf ("l"). F, R-GECO1 and ER-GCaMP6-210 normalized fluorescence changes of the local leaf ("l") over the time after its wounding (red arrow). E, Examples of false-color images illustrate R-GECO1 (magenta) and ER-GCaMP6-210 (green) of a distal leaf of the same wounded plant of (D). G, R-GECO1 and ER-GCaMP6-210 normalized fluorescence changes of a distal leaf ("d") over the time after wounding of "l". H, Maximal peaks of ER-GCaMP6-210 and R-GECO1 fluorescence signals in the local and distal leaves after wounding. I, Time required to reach maximal peaks of ER-GCaMP6-210 and R-GECO1 fluorescence signals in the local and distal leaves after wounding. $n = 5$. L and M, Digitally extracted images of a representative pUBQ10-ER-GCaMP6-210 × pUBQ10-R-GECO1 plant for comparative analyses of the temporal evolution of Ca^{2+} dynamics in the cytosol and ER compartments in response to leaf wounding. L, Temporal analysis of the $\Delta F/F_0$ signal peak in the leaves for the R-GECO1. The temporal window analyzed is of 750 s. The color-bar encodes the time at which the maximum signal is recorded in each pixel. The wounded leaf is colored with blue, since it peaks at around 30 s. The distal leaf is reddish because the maximum signal happens at 500 s. The other two leaves showed a delayed response, at 750 s. M, Same analysis for the ER-GCaMP6-210 as in (L). The wounded leaf responded earlier (200 s, violet) than the distal one (750 s, green). Error bars = SD, $^*P \leq 0.05$, $^{**}P \leq 0.005$ (Student's t test).

dynamics in the ER and cytosol of plant cells. Our data confirm the critical role of the ER as a Ca^{2+} buffering system and provide an unprecedented spatial and temporal resolution of the dynamics of $[Ca^{2+}]_{ER}$ accumulation in different cell types in response to independent external stimuli and during a developmental program. This new technology allows us to demonstrate that, in response to leaf wounding, a long-distance ER Ca^{2+} wave is established, which temporally follows the cytosolic one. This introduces an additional layer of complexity in the rapid long-range signaling in plants (Johns et al., 2021) and opens interesting new scenarios. The generation of this dual sensor line provides the basis for future experiments, feasible at any developmental stage, aimed at identifying critical components involved in the Ca^{2+} transport across ER membranes of plant cells that are essential to shed more light on a still underappreciated role of this compartment in the regulation of local and systemic Ca^{2+} signaling in plants.

Materials and methods

Plant material and growth conditions

All Arabidopsis (*A. thaliana*) plants were of the ecotype Col-0. Seeds were surface-sterilized by vapor-phase sterilization (Clough and Bent, 1998) and plated on half-strength Murashige and Skoog (MS) medium (Murashige and Skoog, 1962; Duchefa, http://www.duchefa-biochemie.com/) supplemented with 0.1% (w/v) sucrose, 0.05% (w/v) 2-(N-morpholino)ethanesulfonic acid (MES), pH 5.8, and 0.8% (w/v) plant agar (Duchefa, http://www.duchefa-biochemie.com/). After stratification at 4°C in the dark for 2 d, plates were transferred to the growth chamber under long-day conditions (16-h light/8-h dark, 100 μE m^{-2} s^{-1} of Cool White Neon lamps) at 22°C. The plates were kept vertically, and seedlings were used for imaging 6 to 7 d after germination (DAG). For imaging in adult plants, 3- to 4-week-old mature plants grown in soil under long-day conditions (16-h light/8-h dark, 100 μE m^{-2} s^{-1} of Cool White Neon lamps) at 22°C and 75% relative humidity were used. *Nicotiana benthamiana* plants were cultivated for 5 to 6 weeks in a greenhouse under a 16-h light/8-h dark cycle with 60% atmospheric humidity and at 22/18°C.

Plant phenotyping and root growth analyses

For whole-plant phenotyping, plants were grown on soil under long-day conditions in individual pots randomly distributed among standard greenhouse flats. Rosettes and siliques were documented photographically. Seeds were harvested from individual siliques and counted. For phenotypic analysis on roots, surface-sterilized seeds were grown vertically on half-strength MS medium supplemented with 0.1% (w/v) sucrose, 0.8% (w/v) plant agar (Duchefa, http://www.duchefa-biochemie.com/), and root length was measured from 3 to 7 DAG. Lengths and sizes were quantified by Fiji (https://imagej.net/Fiji).

Molecular cloning and plasmid constructs

The original plasmid harboring the sequence coding for the ER-GCaMP6-210 (de Juan-Sanz et al., 2017) was obtained from Addgene (https://www.addgene.org/86919/). The *ER-GCaMP6-210* coding sequence was PCR amplified with the Q5 High-Fidelity DNA Polymerase (New England Biolabs, https://www.neb.com/) using the following forward and reverse primers:

AC614 5′-CATGGAATTCATGGGACTGCTGTCTGTGCCT-3′ and
AC615 5′-CATGGGATCCTCACAGCTCATCCTTGCCTCC-3′

harboring the *Eco*RI and *Bam*HI restrictions sites, respectively (underlined). The amplicon was ligated into the empty *Eco*RI/*Bam*HI-digested *pGree0029-Ter* binary vector (Ter corresponds to the 19S CaMV terminator sequence; Hellens et al., 2000; Bonza et al., 2013) to generate the *pGree0029-ER-GCaMP6-210-Ter*. pUBQ10 (Grefen et al., 2010) and pCaMV35S (Amack and Antunes, 2020) promoter sequences were amplified using the following primers:

AC280 5′-CATGGGTACCGTCGACGAGTCAGTAATAAACG-3′;
AC281 5′-CATGGGTACCCTGTTAATCAGAAAAACTCAG-3′;
AC314 5′-CATGGGTACCGATATCGTACCCCTACTCCA-3′; and
AC315 5′-CATGGGTACCGGGCTGTCCTCTCCAAATGAA-3′.

All forward and reverse primers harbor a *Kpn*I restriction site (underlined). The amplicons of both promoters were digested with *Kpn*I and ligated into the *Kpn*I-linearized and dephosphorylated *pGreen0029-ER-GCaMP6-210-Ter* plasmid. The obtained *pGreen0029-pUBQ10-ER-GCaMP6-210-Ter* and *pGreen0029-pCaMV35S-ER-GCaMP6-210-Ter* vectors were sequenced to verify the proper directionality of the inserted promoters and the absence of mistakes. The pGreen0029 vector backbone harbors the *nptI* gene, which confers the resistance to kanamycin in bacteria and the *nptII* gene which confers the resistance to kanamycin in plants (Hellens et al., 2000).

Generation of transgenic plants

The *pGreen0029-pUBQ10-ER-GCaMP6-210* and *pGreen0029-pCaMV35S-ER-GCaMP6-210* constructs were introduced in *Agrobacterium tumefaciens GV3101/pMP90* strain. *Arabidopsis thaliana* Col-0 was transformed by floral-dip (Clough and Bent, 1998). Transgenic lines were selected by the presence of fluorescence for each construct. To obtain the double-sensor lines, the Col-0 pUBQ10-ER-GCaMP6-210 #1 and pCaMV35S-ER-GCaMP6-210 #1 lines were crossed with the Col-0 pUBQ10-R-GECO1 line (Keinath et al., 2015).

Transient expression in *Nicotiana benthamiana* leaves

Leaf infiltration was performed using *A. tumefaciens GV3101/pMP90* strain carrying the specified constructs (pUBQ10-ER-GCaMP6-210-Ter; pCaMV35S-ER-GCaMP6-210-Ter, nWAK2-mCherry-HDEL) together with the p19-enhanced expression system according to the method described by Waadt and Kudla (2008). For the confocal

imaging analysis after the infiltration, the plants were kept for 3–5 d under incubation conditions described above.

Pollen tube growth dynamics

To perform Ca^{2+} imaging analyses during pollen tube growth, pollen grains from 13 to 15 flowering-stage plants were germinated in accordance with Rodriguez-Enriquez et al. (2012) and Schoenaers et al. (2017) (292 mM sucrose, 0.16 mM H_3BO_3, 0.1 mM $CaCl_2$; 0.14 mM $Ca(NO_3)_2$; 0.1 mM KCl, 0.003% [w/v] N-Z-Amine A; 0.055 mM myo-inositol, 0.038 mM ferric ammonium citrate; 0.01 mM spermidine; 10 mM gamma-aminobutyric acid, pH 8.0 adjusted with KOH and 0.5% [w/v] agarose). The solution was heated in a microwave for the agarose to dissolve and cooled down to 50°C–60°C for the pH to be readjusted to pH 8.0. A 0.5 cm × 0.5 cm cellophane membrane (325P cellulose; AA Packaging Limited, Preston, UK) was placed on top of the medium, and pollen grains were placed directly onto the membrane, and the cover glass was flipped on another cover glass that was attached to an opening at the bottom of a small Petri dish. Water was applied on the inner sides of the Petri dish to maintain high humidity and the Petri dish was closed using parafilm. The pollen grains were germinated in a climate-controlled room at 23°C in the dark, and visualized ∼2 h after sample preparation.

Confocal laser scanning microscopy

Confocal microscopy analyses of stable transgenic Arabidopsis seedling root and shoot cells and transiently transformed *N. benthamiana* leaf cells were performed using a Nikon Eclipse Ti2 inverted microscope, equipped with a Nikon A1R+ laser scanning device (http://www.nikon.com/). For localization studies, images were acquired by a CFI Apo Lambda 40XC LWD WI (Numerical Aperture (NA) 1.15) and CFI Plan Apo Lambda 60X Oil (NA 1.4). ER-GCaMP6-210 was excited with the 488-nm laser and the emission was collected at 505–550 nm. R-GECO1 and mCherry were excited with the 561-nm laser and the emission was collected at 570–620 nm. Chlorophyll was excited with the 488-nm laser and the emission was collected at 663–738 nm. The confocal pinhole was set to 20.43 µm and the images were acquired at 2,048 × 2,048 pixels resolution (Figure 1). NIS-Elements (Nikon; http://www.nis-elements.com/) was used as a platform to control the microscope. Images in Figure 1 and Supplemental Figure S2, A–C and G–I were denoised by using the NIS-Element Denoise.ai plugin (https://www.microscope.healthcare.nikon.com/en_EU/products/confocal-microscopes/a1hd25-a1rhd25/nis-elements-ai). Nondenoised images were analyzed using NIS-Elements and Fiji.

Wide-field fluorescence microscopy

For wide-field Ca^{2+} imaging analyses in seedling roots of pUBQ10-ER-GCaMP6-210, pCaMV35S-ER-GCaMP6-210, pUBQ10-R-GECO1, and pCaMV35S-CRT-D4ER lines, an inverted fluorescence Nikon microscope (Ti-E; http://www.nikon.com/) with a CFI Plan Apo VC 20X (NA 0.75) was used. Excitation light was produced by a fluorescent lamp (Prior Lumen 200 PRO; Prior Scientific; http://www.prior.com) set to 20% with 488 nm (470/40 nm) for the ER-GCaMP6-210 sensor, 561 nm (540/25 nm) for the R-GECO1, and 440 nm (436/20 nm) for CRT-D4ER. ER-GCaMP6-210 and R-GECO1 fluorescence emissions were collected at 505–530 and 576–626 nm, respectively. For the analysis of the CRT-D4ER line, the FRET CFP/YFP optical block A11400-03 (emission 1, 483/32 nm for ECFP; emission 2, 542/27 nm for FRET/Citrine) with a dichroic 510 nm mirror (Hamamatsu) was used. Images were collected with a Hamamatsu Dual CCD camera (ORCA-D2; http://www.hamamatsu.com/). Camera binning was set to 2 × 2 for the ER-GCaMP6-210 and R-GECO1, and to 4 × 4 for the CRT-D4ER. Exposure times (from 100 to 400 ms) were adjusted depending on the line analyzed. Images were acquired every 5 s. Filters and the dichroic mirrors were purchased from Chroma Technology (http://www.chroma.com/). NIS-Elements (Nikon; http://www.nis-elements.com/) was used as a platform to control the microscope, illuminator, and camera. Images were analyzed using Fiji.

Spinning disk confocal microscopy

Confocal spinning disk microscopy analyses of root-tip cells and pollen tubes were performed using a Nikon Eclipse Ti2 inverted microscope, equipped with a Yokogawa spinning disk confocal system (https://www.microscope.healthcare.nikon.com/en_EU/products/confocal-microscopes/csu-series/specifications). The oil immersion CFI Plan Apo Lambda 60X Oil (NA 1.4) and the CFI Plan Apo VC 20X (NA 0.75) were used as objectives. ER-GCaMP6-210 was excited by a 488-nm single-mode optical fiber laser and the emission was collected at 525–550 nm. R-GECO1 was excited by a 561-nm single-mode optical fiber laser and the emission was collected at 576–626 nm. Images were collected with a Photometrics Prime BSI CMOS camera (https://www.photometrics.com/products/prime-family/primebsi/) with an exposure time of 200–300 ms with a 2 × 2 binning (1,024 × 1,024 pixels) for each emission.

For dynamic Ca^{2+} imaging analyses, images were acquired every 2 or 5 s. The NIS-Elements AR (Nikon, Japan, http://www.nis-elements.com/) was used as a platform to control the microscope, laser, camera, and postacquisition analyses. Images in Figures 2, 3 were denoised by using the NIS-Elements Denoise.ai plugin (https://www.microscope.healthcare.nikon.com/en_EU/products/confocal-microscopes/a1hd25-a1rhd25/nis-elements-ai). Raw nondenoised images were analyzed using Fiji.

Wound-induced calcium imaging in adult plants

Adult plants of pUBQ10-ER-GCaMP6-210 × pUBQ10-R-GECO1 were imaged with a Nikon stereomicroscope (SMZ18, http://www.nikon.com/) equipped with a 5.9 megapixel CMOS DS-Fi3 Microscope Camera. Excitation light was produced by a mercury light source (Intensilight; http://www.nikon.com/) with GFP and RFP filter cubes. A Plan Apo 0.5X objective was used without zoom for the imaging of the entire plant and images were collected with an

exposure time of 1 s with a 2 × 2 camera binning (1,440 × 1,024 pixels) for each emission. R-GECO1 and ER-GCaMP6-210 images were acquired every 10 s by manually switching between the GFP and RFP configuration. During the entire experiment, plants were continuously illuminated.

Seedling imaging

Seven-day-old seedlings were used for root imaging. For root experiments, seedlings were kept in the growth chamber until the experiment and gently removed from the plate according to Behera and Kudla (2013), placed in the dedicated chambers and overlaid with cotton wool soaked in imaging solution (5 mM KCl, 10 mM MES, 10 mM $CaCl_2$ pH 5.8 adjusted with Tris–base). The root was continuously perfused with imaging solution using a perfusion pump (Behera et al., 2018), while the shoot was not submerged. Treatments were carried out by supplementing the imaging solution with 0.1 mM Na_2ATP (sodium ATP; from a 200 mM stock solution buffered at pH 7.4 with NaOH), 0.01 mM NAA (from a 10.74 mM stock solution), or 25 μM of CPA (from a 10 mM stock solution dissolved in 100% [v/v] DMSO) administered for 3 min under continuous perfusion.

Quantitative imaging analysis

Fluorescence intensity was determined over ROIs, which corresponded to: (1) cells of the meristematic and transition zone of seedling root tips (wide-field microscope); (2) single meristematic root-tip cells (spinning disk microscope); (3) pollen tube tip or shank (spinning disk microscope); and (4) wounded and unwounded leaves of adult plants (stereomicroscope). ER-GCaMP6-210 and R-GECO1 emissions of the analyzed ROIs were used for single fluorescence emissions analyses. Citrine and ECFP emissions of CRT-D4ER of the analyzed ROIs were used for the ratio (R) calculation (Citrine/ECFP). Background subtraction was performed in all experiments, except in those performed with adult plants imaged with the stereomicroscope. Fluorescence (F) and ratio (R) values at different time points were normalized to the initial fluorescence (F_0) ($\Delta F/F_0$) or ratio (R_0) ($\Delta R/R_0$) and plotted versus time. For pollen experiments, the fluorescence emissions were normalized as (X − mean)/SD. Where X is the fluorescence value at a given time point, mean and SD are respectively the average fluorescence value of all the time points and the associated standard deviation. The analysis of fluorescent intensities was in all cases performed on raw nondenoised images.

Pollen tubes registration and growth analysis

To quantify the tip Ca^{2+} oscillations in pollen tubes, we applied a semi-automatic routine to register the image stacks taken at different times. The registration of each ROI was performed by computing the cross-correlation between each couple of consecutive images. In this way, the pollen tube apex was maintained at the same position. This computation was performed with the Fiji plugin 'Template Matching' (https://sites.google.com/site/qingzongtseng/template-matching-ij-plugin) after selecting the pollen tube apex as a landmark and using a subpixel cross-correlation method. The horizontal and vertical displacements were stored, and the process was iterated for all time points. The average speed of the pollen tube growth was obtained by dividing the total elongation by the time.

Kymograph

To evaluate the pollen tube elongation, we used a graphical method for a space-time representation of the pollen tube tip evolution. We draw a spatial path that follows the tip of the tube during its growth, as observed in the entire image sequence (x,y,t). By using the Fiji "Dynamic Reslice" function, we create a new image, which depicts the temporal evolution of the pollen elongation through the spatial path previously defined.

Cross-correlation analyses of fast fluctuations

To evaluate the temporal delay between the two fluorescent channels, we performed a signal analysis based on cross-correlation. To understand the correlation between the fast oscillations occurring in both the R-GECO1 and ER-GCaMP6-210, we used a statistical approach based on the data acquired in the set of nine independent measurements. First, we removed the slow dynamics in each signal, estimated by subtracting a low-pass version of the temporal signature. Such a low-pass version was obtained by filtering the signal with a Gaussian kernel of sigma $\sigma = 80$ s. Consecutively, each curve obtained was examined by running cross-correlation analysis in sliding windows of 80 s, with a stride of 2 s. Within each temporal window, we normalized the signal by its SD and subtracted the mean. In this way, we could calculate the normalized version of the cross-correlation. This analysis was repeated by striding the window through the entire signal duration for all the measurements and let us estimate the average cross-correlation and its associated error. The temporal location of the peaks indicates an average temporal delay between the two signals.

Temporal representation of Ca^{2+} waves in mature plants

To produce a visual representation of the overall temporal propagation of the Ca^{2+} signals in the whole plant, we first removed a common background in the images, segmenting the plant (by thresholding) and setting to zero the values outside of the plant. We then realigned each time point of the same leaf by selecting a region that enclosed it. In the successive frames, we compensated for the movement by evaluating the cross-correlation displacement. In this way, the intensity in each pixel described the temporal evolution of the signal in a given position within the leaf. Once each leaf was spatially realigned for the entire duration of the acquisition, it was possible to compute the $\Delta F/F_0$ on the full image sequence. To obtain a visual image that describes the temporal propagation by using a false-color representation, we mapped the temporal location of the maximum intensity in each pixel with a color in the look-up table. The color intensity was chosen to be proportional to the peak

intensity found in the temporal evolution of the pixel. In this representation, the blue color indicates that the peak intensity was achieved at early timings, fading to red and green for middle and late timings, respectively.

Statistical analysis

All the data are representative of $n \geq 4$ experiments. Reported traces are the averages of traces from all single experiments used for the statistical analyses. Results are reported as averages $\pm$ SD. *P*-values were calculated with an unpaired Student's *t* test. Data from experiments with at least $n = 5$ were plotted as box-and-whisker plots using GraphPad, in which all the experimental points are plotted, and their distribution represented as a box that extends from the 25th to 75th percentiles. The line in the middle of the box is plotted at the median.

Supplemental data

The following materials are available in the online version of this article.

Supplemental Figure S1. Subcellular distribution of ER-GCAMP6-210 in *N. benthamiana* leaf epidermal cells.

Supplemental Figure S2. Confocal microscopy analyses revealed efficient ER-GCaMP6-210 expression in different organs of Arabidopsis stable transgenic pUBQ10-ER-GCaMP6-210.

Supplemental Figure S3. Cytosolic and ER Ca^{2+} transients in root-tip cells of Arabidopsis seedlings expressing the R-GECO1 (cytosolic and nuclear localized) and ER-GCaMP6-210 (ER localized) sensors in response to external ATP (0.1 mM) and NAA (0.01 mM), and Cameleon CRT-D4ER (ER localized) in response to external ATP (0.1 mM).

Supplemental Figure S4. Coexpression of ER-GCaMP6-210 and R-GECO1 in guard cells.

Supplemental Figure S5. Plant development is unchanged in the generated calcium indicators lines.

Supplemental Movie S1. Movie from a representative time series of a WT Arabidopsis seedling root tip expressing the ER-GCaMP6-210 (green) and R-GECO1 (magenta) sensors in response to external ATP. Scale bar: 15 µm.

Supplemental Movie S2. Movie from two representative time series of WT Arabidopsis pollen tubes expressing the ER-GCaMP6-210 (green) and R-GECO1 (magenta) sensors. Scale bar: 20 µm.

Supplemental Movie S3. Movie from a representative time series of a WT Arabidopsis mature plant expressing the ER-GCaMP6-210 (green) and R-GECO1 (magenta) sensors in response to leaf wounding. Scale bar: 1 mm.

Acknowledgments

We thank Dr Melanie Krebs (University of Heidelberg) for providing us the pUBQ10-R-GECO1 Arabidopsis line, and Prof. Kris Vissemberg and Dr Sébastjen Schoenaers (University of Antwerp) for their training in the pollen tube growth assays. Imaging analyses were carried out at NOLIMITS, an advanced imaging facility established by the University of Milan. Plant transformation and selection were supported by the "Piattaforma Piante" from the Department of Biosciences at the University of Milan.

Funding

This work was supported by Piano di Sviluppo di Ateneo 2019 (University of Milan to A.C.), by Ministero dell'Istruzione, dell'Università e della Ricerca Fondo per Progetti di ricerca di Rilevante Interesse Nazionale 2017 (PRIN 2017ZBBYNC to M.C.B.), and by a PhD fellowship from the University of Milan (to M.G.). We acknowledge fundings from H2020 Marie Skłodowska-Curie Actions (HI-PHRET project, 799230 to D.A.).

Conflict of interest statement. The authors have declared that no conflict of interests exist.

References

Aller I, Rouhier N, Meyer AJ (2013) Development of roGFP2-derived redox probes for measurement of the glutathione redox potential in the cytosol of severely glutathione-deficient rml1 seedlings. Front Plant Sci **16**: 506.

Amack SC, Antunes MS (2020) CaMV35S promoter—a plant biology and biotechnology workhorse in the era of synthetic biology. Curr Plant Biol **24**: 100179

Baird GS, Zacharias DA, Tsien RY (1999) Circular permutation and receptor insertion within green fluorescent proteins. Proc Natl Acad Sci U S A **96**: 11241–11246

Barberini ML, Sigaut L, Huang W, Mangano S, Juarez SPD, Marzol E, Estevez J, Obertello M, Pietrasanta L, Tang W, et al. (2018) Calcium dynamics in tomato pollen tubes using the Yellow Cameleon 3.6 sensor. Plant Reprod **31**:159–169

Behera S, Kudla J (2013) High-resolution imaging of cytoplasmic Ca^{2+} dynamics in Arabidopsis roots. Cold Spring Harb Protoc **2013**: 665–669

Behera S, Xu Z, Luoni L, Bonza MC, Doccula FG, De Michelis MI, Morris RJ, Schwarzländer M, Costa A (2018) Cellular Ca^{2+} signals generate defined pH signatures in plants. Plant Cell **30**: 2704–2719

Bonza MC, De Michelis MI (2011). The plant Ca^{2+}-ATPase repertoire: biochemical features and physiological functions. Plant Biol **13**: 421–430

Bonza MC, Loro G, Behera S, Wong A, Kudla J, Costa A (2013). Analyses of Ca^{2+} accumulation and dynamics in the endoplasmic reticulum of Arabidopsis root cells using a genetically encoded Cameleon sensor. Plant Physiol **163**: 1230–1241

Brandizzi F, Fricker M, Hawes C (2002) A greener world: the revolution in plant bioimaging. Nat Rev Mol Cell Biol **3**: 520–530

Charpentier M, Sun J, Vaz Martins T, Radhakrishnan GV, Findlay K, Soumpourou E, Thouin J, Very AA, Sanders D, Morris RJ, et al. (2016) Nuclear-localized cyclic nucleotide-gated channels mediate symbiotic calcium oscillations. Science **352**: 1102–1105

Chen TW, Wardill TJ, Sun Y, Pulver SR, Renninger SL, Baohan A, Schreiter ER, Kerr RA, Orger MB, Jayaraman V, et al. (2013) Ultrasensitive fluorescent proteins for imaging neuronal activity. Nature **499**: 295–300

Clough SJ, Bent AF (1998) Floral dip: a simplified method for Agrobacterium-mediated transformation of *Arabidopsis thaliana*. Plant J **16**: 735–743

Corso M, Doccula FG, de Melo JRF, Costa A, Verbruggen N (2018) Endoplasmic reticulum-localized CCX2 is required for osmotolerance by regulating ER and cytosolic Ca^{2+} dynamics in Arabidopsis. Proc Natl Acad Sci U S A **115**: 3966–3971

Costa A, Candeo A, Fieramonti L, Valentini G, Bassi A (2013) Calcium dynamics in root cells of Arabidopsis thaliana visualized with selective plane illumination microscopy. PLoS One **8**: e75646.

Damineli DSC, Portes MT, Feijó JA (2017) Oscillatory signatures underlie growth regimes in Arabidopsis pollen tubes: computational methods to estimate tip location, periodicity, and synchronization in growing cells. J Exp Bot **68**: 3267–3281

De Col V, Fuchs P, Nietzel T, Elsässer M, Voon CP, Candeo A, Seeliger I, Fricker MD, Grefen C, Møller IM, et al. (2017) ATP sensing in living plant cells reveals tissue gradients and stress dynamics of energy physiology. eLife **6**: e26770

de Juan-Sanz J, Holt GT, Schreiter ER, de Juan F, Kim DS, Ryan TA (2017) Axonal endoplasmic reticulum Ca^{2+} content controls release probability in CNS nerve terminals. Neuron **93**: 867–881

Edel KH, Marchadier E, Brownlee C, Kudla J, Hetherington AM (2017) The evolution of calcium-based signaling in plants. Curr Biol **27**: R667–R679

Feijó JA, Costa SS, Prado AM, Becker JD, Certal AC (2004) Signalling by tips. Curr Opin Plant Biol **7**: 589–598

Foskett JK, White C, Cheung KH, Mak DO (2007) Inositol trisphosphate receptor Ca^{2+} release channels. Physiol Rev **87**: 593–658

Franklin-Tong VE, Drobak BK, Allan AC, Watkins P, Trewavas AJ (1996) Growth of pollen tubes of Papaver rhoeas is regulated by a slow-moving calcium wave propagated by inositol 1,4,5-trisphosphate. Plant Cell **8**: 1305–1321

Grefen C, Donald N, Hashimoto K, Kudla J, Schumacher K, Blatt MR (2010) A ubiquitin-10 promoter-based vector set for fluorescent protein tagging facilitates temporal stability and native protein distribution in transient and stable expression studies. Plant J **64**: 355–365

Greotti E, Wong A, Pozzan T, Pendin D, Pizzo P (2016) Characterization of the ER-targeted low affinity Ca^{2+} probe D4ER. Sensors (Basel) **16**: 1419

Hellens RP, Edwards EA, Leyland NR, Bean S, Mullineaux PM (2000) pGreen: a versatile and flexible binary Ti vector for Agrobacterium-mediated plant transformation. Plant Mol Biol **42**: 819–832

Holdaway-Clarke TL, Feijo JA, Hackett GR, Kunkel JG, Hepler PK (1997) Pollen tube growth and the intracellular cytosolic calcium gradient oscillate in phase while extracellular calcium influx is delayed. Plant Cell **9**: 1999–2010

Iwano M, Entani T, Shiba H, Kakita M, Nagai T, Mizuno H, Miyawaki A, Shoji T, Kubo K, Isogai A, et al. (2009) Fine-tuning of the cytoplasmic Ca^{2+} concentration is essential for pollen tube growth. Plant Physiol **150**: 1322–1334

Ishka MR, Brown E, Rosenberg A, Romanowsky S, Davis J, Choi W-G, Harper JF (2021) Arabidopsis Ca^{2+}-ATPases 1, 2, and 7 in the endoplasmic reticulum contribute to growth and pollen fitness. Plant Physiol **185**: 1966–1985

Johns S, Hagihara T, Toyota M, Gilroy S (2021) The fast and the furious: rapid long-range signaling in plants. Plant Physiol **185**: 694–706

Keinath NF, Waadt R, Brugman R, Schroeder JI, Grossmann G, Schumacher K, Krebs M (2015) Live cell imaging with R-GECO1 sheds light on flg22- and chitin-induced transient $[Ca^{2+}]_{cyt}$ patterns in Arabidopsis. Mol Plant **8**: 1188–1200

Leitão N, Dangeville P, Carter R, Charpentier M (2019) Nuclear calcium signatures are associated with root development. Nat Commun **10**: 4865

Li K, Prada J, Damineli DSC, Liese A, Romeis T, Dandekar T, Feijó JA, Hedrich R, Konrad KR (2021) An optimized genetically encoded dual reporter for simultaneous ratio imaging of Ca^{2+} and H^+ reveals new insights into ion signaling in plants. New Phytol **230**: 2292–2310

Liang F, Sze H (1998) A high-affinity Ca^{2+} pump, ECA1, from the endoplasmic reticulum is inhibited by cyclopiazonic acid but not by thapsigargin. Plant Physiol **118**: 817–825

Lovy-Wheeler A, Cárdenas L, Kunkel JG, Hepler PK (2007) Differential organelle movement on the actin cytoskeleton in lily pollen tubes. Cell Motil Cytoskeleton **64**: 217–232

Luo J, Chen L, Huang F, Gao P, Zhao H, Wang Y, Han S (2020) Intraorganellar calcium imaging in Arabidopsis seedling roots using the GCaMP variants GCaMP6m and R-CEPIA1er. J Plant Physiol **246–247**: 153127

Martinière A, Bassil E, Jublanc E, Alcon C, Reguera M, Sentenac H, Blumwald E, Paris N (2013) *In vivo* intracellular pH measurements in tobacco and Arabidopsis reveal an unexpected pH gradient in the endomembrane system. Plant Cell **25**: 4028–4043

Mousavi SA, Chauvin A, Pascaud F, Kellenberger S, Farmer EE (2013) GLUTAMATE RECEPTOR-LIKE genes mediate leaf-to-leaf wound signalling. Nature **500**: 422–426

Murashige T, Skoog F (1962) A revised medium for rapid growth and bioassays with tobacco tissue cultures. Physiol Plant **15**: 473–497

Navazio L, Bewell MA, Siddiqua A, Dickinson GD, Galione A, Sanders D (2000) Calcium release from the endoplasmic reticulum of higher plants elicited by the NADP metabolite nicotinic acid adenine dinucleotide phosphate. Proc Natl Acad Sci U S A **97**: 8693–8698

Nagai T, Yamada S, Tominaga T, Ichikawa M, Miyawaki A (2004) Expanded dynamic range of fluorescent indicators for Ca^{2+} by circularly permuted yellow fluorescent proteins. Proc Natl Acad Sci U S A **101**: 10554–10559

Nakai J, Ohkura M, Imoto K (2001) A high signal-to-noise Ca^{2+} probe composed of a single green fluorescent protein. Nat Biotechnol **19**: 137–141

Nelson BK, Cai X, Nebenführ A (2007) A multicolored set of *in vivo* organelle markers for co-localization studies in Arabidopsis and other plants. Plant J **51**: 1126–1136

Nguyen CT, Kurenda A, Stolz S, Chételat A, Farmer EE (2018) Identification of cell populations necessary for leaf-to-leaf electrical signaling in a wounded plant. Proc Natl Acad Sci U S A **115**: 10178–10183

Palmer AE, Giacomello M, Kortemme T, Hires SA, Lev-Ram V, Baker D, Tsien RY (2006) Ca^{2+} indicators based on computationally redesigned calmodulin-peptide pairs. Chem Biol **13**: 521–530

Peragine A, Yoshikawa M, Wu G, Albrecht HL, Poethig RS (2004) SGS3 and SGS2/SDE1/RDR6 are required for juvenile development and the production of trans-acting siRNAs in Arabidopsis. Genes Dev **18**: 2368–2379

Resentini F, Ruberti C, Grenzi M, Bonza MC, Costa A (2021) The signatures of organellar calcium. Plant Physiol doi. 10.1093/plphys/kiab189

Rodriguez-Enriquez M, Mehdi S, Dickinson H, Grant-Downtown R (2012) A novel method for efficient *in vitro* germination and tube growth of Arabidopsis thaliana pollen. New Phytol **197**: 668–679

Schoenaers S, Balcerowicz D, Costa A, Vissenberg K (2017) The kinase ERULUS controls pollen tube targeting and growth in *Arabidopsis thaliana*. Front Plant Sci **8**: 1942

Shkolnik D, Nuriel R, Bonza MC, Costa A, Fromm H (2018) MIZ1 regulates ECA1 to generate a slow, long-distance phloem-transmitted Ca^{2+} signal essential for root water tracking in Arabidopsis. Proc Natl Acad Sci U S A **115**: 8031–8036

Soboloff J, Rothberg BS, Madesh M, Gill DL (2012) STIM proteins: dynamic calcium signal transducers. Nat Rev Mol Cell Biol **13**: 549–565

Tanaka K, Swanson SJ, Gilroy S, Stacey G (2010) Extracellular nucleotides elicit cytosolic free calcium oscillations in Arabidopsis. Plant Physiol **154**: 705–719

Tian D, Wang J, Zeng X, Gu K, Qiu C, Yang X, Zhou Z, Goh M, Luo Y, Murata-Hori M, et al. (2014) The rice TAL effector-dependent resistance protein XA10 triggers cell death and calcium depletion in the endoplasmic reticulum. Plant Cell **26**: 497–515

Toyota M, Spencer D, Sawai-Toyota S, Jiaqi W, Zhang T, Koo AJ, Howe GA, Gilroy S (2018) Glutamate triggers long-distance, calcium-based plant defense signaling. Science **361**: 1112–1115

Vigani G, Costa A (2019) Harnessing the new emerging imaging technologies to uncover the role of Ca^{2+} signaling in plant nutrient homeostasis. Plant Cell Environ **42**: 2885–2901

Vincent TR, Avramova M, Canham J, Higgins P, Bilkey N, Mugford ST, Pitino M, Toyota M, Gilroy S, Miller AJ, et al. (2017) Interplay of plasma membrane and vacuolar ion channels, together with BAK1, elicits rapid cytosolic calcium elevations in Arabidopsis during aphid feeding. Plant Cell **29**: 1460–1479

Waadt R, Krebs M, Kudla J, Schumacher K (2017) Multiparameter imaging of calcium and abscisic acid and high-resolution quantitative calcium measurements using R-GECO1-mTurquoise in Arabidopsis. New Phytol **216**: 303–320

Waadt R, Kudla J (2008) In planta visualization of protein interactions using bimolecular fluorescence complementation (BiFC). Cold Spring Harb Protoc **2008**: pdb.prot4995

Zhao Y, Araki S, Wu J, Teramoto T, Chang YF, Nakano M, Abdelfattah AS, Fujiwara M, Ishihara T, Nagai T, et al. (2011) An expanded palette of genetically encoded Ca^{2+} indicators. Science **333**: 1888–1891